Through-Thickness Texture Gradients in Rolled Polycrystalline Alloys

by S. E. Schoenfeld
and R. J. Asaro

October 1997

19971201 061

DTIC QUALITY INSPECTED 4

Army Research Laboratory
Aberdeen Proving Ground, MD 21005-5066

ARL-TR-1531 October 1997

Through-Thickness Texture Gradients in Rolled Polycrystalline Alloys

S. E. Schoenfeld
Weapons and Materials Research Directorate, ARL

R. J. Asaro
Department of Applied Mechanics and Engineering Science
University of California, San Diego

Abstract

A simple and accurate approach to modeling deformation processes that are highly constrained by boundary conditions is presented. The method involves a detailed finite element analysis of the most controlling aspects of the process. Additional analysis of the material states of texture and anisotropy are calculated as deemed necessary. The method is applied to the rolling process with a detailed analysis of the rolling of aluminum sheet. Particular attention is paid to the analysis of the roll-gap geometry and the transfer of tractions from the roll to the workpiece. The calculated deformation state is then applied to a more detailed calculation of material texture, which tracks the motion of individual crystallites due to macroscopic boundary conditions. The method allows not only a detailed analysis of through-thickness texture gradients, but also a detailed description of the boundary conditions and deformation states that cause such textures. The macroscopic anisotropy resulting from such textures is investigated, and the use of the method as a process design tool is discussed. Finally, results are compared to experimentally determined through-thickness texture gradients in rolled aluminum alloys, and details concerning the general roll-gap deformation field are discussed.

Acknowledgments

INTENTIONALLY LEFT BLANK

Table of Contents

INTENTIONALLY LEFT BLANK

List of Figures

INTENTIONALLY LEFT BLANK

1. Introduction

During the process of sheet rolling, a billet or workpiece is passed under a roll that compresses and shears the material. Although the workpiece may be pushed or pulled under the roll, it is the interaction with the spinning roll that adds varying through-thickness shear deformations to the workpiece and thus destroys homogeneity through the cross section. These gradients in through-thickness deformation, along with the resulting differences in material state such as texture and anisotropy, are important with regard to the material's constitutive properties and mechanical behavior during subsequent forming processes such as sheet bending or drawing.

During deep drawing, for example, texture-induced anisotropy is the cause of nonuniformity in the height of the rim above the base in cups punched from rolled polycrystalline sheet. Optimum drawability (i.e., the maximum depth to which a cup can be drawn while minimizing anomalies in the height [known as *ears*]) has been defined and interpreted with respect to texture by Lequeu and Jonas (1988), while Nelson and Fricke (1988) have correlated particular textures with the behavior of ears on cups drawn from rolled sheet.

Another example includes the necking of thin rolled sheets. Hill (1950) described the inclination of such necks away from the rolling direction based on macroscopic anisotropy due to rolling. Still another example was provided by Asaro and Needleman (1985) who incorporated textural effects into calculations of localization in biaxially stretched sheets and were able to develop forming-limit diagrams for textured polycrystalline sheet.

Accordingly, the purpose of the present work is to develop a relatively simple, but accurate approach to modeling deformation processes, such as rolling, for the purpose of predicting deformation and material states. Our intentions for rolling are to concentrate on understanding the effects of boundary constraints such as are imposed by the geometry of the roll-workpiece contact zone and the friction that develops between them. With this in mind, we sought a particularly efficient approach with the additional aim that it might be directly useful in designing rolling processes. Such an approach will also allow for the effort to be placed on what are deemed the most controlling aspects of the process; whereas, additional detail regarding material constitutive description or material failure mechanisms may be added as they are judged to be necessary.

The roll-workpiece interaction complicates the deformation state in at least two fundamental ways. The first is by frictional interaction. Shear stresses along the workpiece boundary have been experimentally connected to the development of inhomogeneous through-thickness texture (and thus to displacement fields) by Truszkowski, Krol, and Major (1980); Truszkowski and Kiel (1980); Asbeck and Mecking (1978); and Dillamore and Roberts (1963) among others. Most authors agree that this effect is limited to a shallow surface layer. For example, Asbeck and Mecking (1978) studied through-thickness variation in rolled copper single crystals. The initial orientation of the crystals were chosen such that the orientation would remain stable during plane-strain compression. In rolling such crystals, deviations from the plane-strain compressive state would be detected by a change in the orientation of the single crystal. They found that the influence of friction is only of minor importance away from a small surface layer. Second, and perhaps more significant, substantial penetration of shear

1

deformation into the cross section can be found as an effect of roll-gap geometry, in particular, during what has become known as small draught rolling. Small draught rolling is characterized by the previously cited authors as the ratio $l_c/h \leq 0.5$, where l_c is the length of contact between the roll and workpiece, and h is the initial thickness of the workpiece. Asbeck and Mecking's (1978) experiments showed that the orientation of the rolled single crystals became more inhomogeneous through the thickness as l_c/h became less than 0.5. Our simulations, in fact, reflect their experimental results in that we find frictional effects are limited to the surface of the workpiece, and large inhomogeneous texture gradients develop as the ratio l_c/h decreases. In what follows, we compare our predicted polycrystal textures to the experimental results of Dillamore and Roberts (1963) and Truszkowski, Krol, and Major (1980) and find that we are able to predict through-thickness textural gradients in rolled polycrystal aggregates.

In previous analytical investigations into textural development in polycrystal aggregates, the rolling process has often been idealized as plane-strain compression. Although agreement between plane-strain textures and textures measured from the center of rolled specimens have been found experimentally by Truszkowski, Krol, and Major (1980); Truszkowski and Kiel (1980); and Dillamore and Roberts (1963), a more detailed analysis of the roll gap is required in order to resolve textures away from the center of rolled materials. In the previously mentioned experiments, it is found that textures through the thickness of the workpiece vary from those characteristic of plane-strain compression in the center of the sheet to a mixture of compression and shear textures at the sheet surface and that the textural gradients vary according to the previously mentioned rolling conditions. Our simulations reflect these trends and add insight to the deformation states that cause these textures to occur.

In order to accurately resolve the roll-gap displacement field, we have conducted finite element analyses of the rolling process. Special attention has been paid to the frictional boundary conditions and the description and control of the roll-gap geometry. Our plan was to use a reasonably accurate, but computationally efficient global constitutive model to approximate macroscopic aggregate behavior during the rolling process. To this end, we have used a version of the phenomenological constitutive theory developed by Bammann (1990) that has been shown to give predictions for multiaxial stress vs. strain response that is consistent with those given by Asaro and Needleman's (1985) polycrystal model based on crystallographic slip theory (Schoenfeld et al. 1991). Once the displacement time history of the roll gap has been calculated, a more detailed analysis can be conducted at arbitrary locations of interest through the thickness of the workpiece that, *inter alia*, calculates texture, material anisotropy, and more detailed material constitutive behavior. For this purpose, we have used the elastic-plastic polycrystal model developed by Asaro and Needleman (1985). We believe the procedure to be highly efficient and, as is indicated by the comparisons to experiment presented section 5, quite accurate. With regard to the apparent accuracy of our approach, we suspect it is primarily due to the fact that in processes such as rolling, deformation fields are strongly constrained and determined by boundary conditions; this would then underscore our decision to pay particular attention to the constraints imposed by contact and friction.

We note that other approaches have been tried to model microstructural changes within formed polycrystalline parts, in particular those that have used slip theories, *per se*, to model the constitutive theory. For example, Kalidindi, Bronkhorst, and Anand (1991) have implemented Asaro and Needleman's (1985) polycrystal model within the finite element code ABAQUS (Hibbit, Karlsson, and Sorensen 1988) and have carried out simulations of simple deformation processes such as simple shear and plane-strain forging. Mathur and Dawson (1989) have likewise used existing models of this kind to simulate plane-strain rolling; their analysis, however, did not concentrate on the effects of boundary constraints as done here. Implementation of such theories is, of course, quite standard and straightforward nowadays, especially since these versions of crystal slip theory were originally formulated for finite element analyses (e.g., Pierce, Asaro, and Needleman 1983; Harren, Deve, and Asaro, 1988). They are not, however, likely to lead to additional insight in problems where the overall fields are so strongly influenced by boundary constraints.

The plan of the paper is as follows. Section 2 is concerned with the description of the finite element analysis of rolling. The contact algorithm used is described in section 2.1, the friction model in section 2.2, the phenomenological constitutive model in section 2.3, and the finite element model overall in section 2.4. In section 3, the texture analysis is described. The computed results are presented in section 4, and discussion and conclusions follow in section 5.

2. Boundary Conditions

The idealization of the rolling process as plane-strain compression has, in the past, been motivated by attempts to provide a simple description of the deformation state. The plane-strain compression boundary conditions were first idealized by prescribing only equivalent principal strains in the directions perpendicular to the compressive axis. For the purpose of analyzing texture development, Asaro and Needleman (1985) later described the plane-strain compressive state as a combination of both tractions and deformations and then solved the mixed-boundary value problem. The success of this method was that it removed the constraints imposed on the constitutive model by simpler displacement-only descriptions of the boundary value problem. The limitations of the model, of course, were that applied displacement fields and tractions must be known, a priori, thus restricting analysis to simple deformation states.

In an attempt to model the combined compression/shear deformation state found during rolling, Lee and Duggan (1991) added a component of shear to the macroscopic velocity gradient that they imposed on an aggregate. This deformation state was considered uniform through the thickness, and no attempt to resolve actual inhomogeneities for any particular roll gap was made. In the analysis that follows, a detailed finite element formulation is used to resolve macroscopic boundary conditions throughout the roll gap.

The boundary conditions for the polycrystal aggregate calculation are extracted from a finite element analysis using a modified version of DYNA2D. The explicit, 2-D vectorized finite element code is ideal for analyzing the large-strain dynamic response of inelastic solids. It

contains a contact-impact algorithm that is ideally suited toward our analysis. Our modifications to the code include implementation of an advanced friction model for friction at high normal pressure and a physically motivated internal variable constitutive model to give a reasonable approximation to global polycrystal aggregate behavior. These modifications, along with a precursor description of DYNA2D's contact algorithm, are documented in the following sections.

2.1 Contact Algorithm

The tractions arising from the roll-workpiece contact are of paramount importance in calculating the boundary conditions applied to the polycrystal aggregate. In order to describe the roll-gap geometry accurately, the model must include an elastically deformable roll. This being the case, the geometry of the imposed traction boundary condition is not known prior to rolling, and tractions must be imposed through the use of a contact algorithm that can accommodate the transfer of tractions from the deformable roll to the workpiece. Input to the model will include a list of nodes on the surface of the roll (master nodes) and nodes on the surface of the workpiece (slave nodes). Initial conditions will include only a description of the rolling motion of the tool. Displacements in the workpiece occur due to the transmission of normal and shear forces from the roll to the workpiece via the contact algorithm.

After an increment of displacement, a search is performed to determine if any particular slave nodes have penetrated into any particular master segments (i.e., elements containing master nodes). In the event of a slave penetration into a master segment, the distance of penetration, l, in the direction normal to the surface, $\mathbf{m}$, is calculated. A restoring force, $\mathbf{q}$, is applied to the affected degrees of freedom to restore the node to the interface surface. The restoring force is calculated by approximating the interface by a series of elastic springs; it has become known as the penalty method (Kiuchi and Oden 1986). The force applied to the slave node perpendicular to the interface is a function of the penetration distance and stiffness coefficient, k, based on the elements that contain the node. In particular,

$$\mathbf{q} = kl\mathbf{m}, \tag{1}$$

and

$$k = pK_iA_i^2/V_i. \tag{2}$$

In equations (1) and (2), K_i is the bulk modulus, A_i is the segment area, V_i is the volume of the ith element that contains the node, and p is the penalty scale factor (taken here to have a value of 0.10). For each element, k is calculated on the slave surface that contains the node and then averaged.

Friction is then included into the algorithm as in Benson and Hallquist (1990). The maximum permissible frictional force, $\mathbf{Q}_{max}$, is obtained from

$$\mathbf{Q}_{max} = \Psi(\mathbf{q}), \tag{3}$$

where $\Psi(\mathbf{q})$ returns the maximum allowable frictional force based upon the normal force; this is discussed in the next section. A trial force, $\mathbf{q}^t$, is calculated based on a displacement

increment of the slave node along the master interface segment, $\Delta \mathbf{x}$ (Benson and Hallquist 1990), and the force vector associated with the node from the last time step, $\mathbf{q}^n$, as

$$\mathbf{q}^t = \mathbf{q}^n - K\Delta \mathbf{x} \ . \tag{4}$$

The new force vector associated with the node, $\mathbf{q}^{n+1}$, will be

$$\mathbf{q}^{n+1} = \mathbf{q}^t \quad \text{if} \quad |\mathbf{q}^t| \leq \mathbf{Q}_{max}, \tag{5}$$

or

$$\mathbf{q}^{n+1} = \mathbf{Q}_{max} \cdot \frac{\mathbf{q}^t}{|\mathbf{q}^t|} \quad \text{if} \quad \mathbf{q}^t > \mathbf{Q}_{max} \ . \tag{6}$$

The total force on the slave node is now the sum of the normal and the tangential forces,

$$\mathbf{Q} = \mathbf{q} + \mathbf{q}^{n+1}, \tag{7}$$

while an equal and opposite force is distributed to the nodes of the master segment via the element interpolation functions.

2.2 Friction Model

The frictional conditions encountered within the roll gap vary both temporally at any particular point along the interface and spatially along the contact length. During the initial phase of the rolling process, the contact length is small and shear stresses along the interface work to drag the workpiece under the roll. As the contact length grows, the workpiece also accelerates, and its velocity relative to the roll also changes. Normal stresses become quite high (four to five times the material yield stress depending on the roll-gap geometry), and a standard assumption of Coulomb friction would yield unrealistically high frictional forces as follows from Wanheim (1973) and Durham and Assempoor (1990). The friction model chosen here is taken from Wanheim (1973) and Wanheim and Bay (1978). The model is based on a physical picture of flattening of surface asparities and the change of real vs. apparent area of contact with increasing normal pressure. For low normal pressure, Wanheim and Bay's expression leads to a linear proportionality between shear stress and normal pressure. As the normal pressure increases, the shear stress eventually saturates to a fraction of the yield stress in simple shear. This saturation shear stress is based on the fraction of full-sticking in the real area of contact. Since Wanheim and Bay's expression was derived for an ideally plastic material, the results are not directly applicable, and we use the modification of the original expression due to Richelsen (1991). Here, we approximate the yield stress in pure shear as $\sigma_o/\sqrt{3}$, where σ_o is the material flow stress in pure tension. The modification of Wanheim and Bay's result due to Richelsen yields an expression for the maximum allowable shear stress during frictional sliding, vis.;

$$T_t(T_n) = \begin{cases} \mu T_n & \text{if } T_n \leq T'_n \\ T'_t + (f\sigma_o/\sqrt{3} - T'_t)(1 - \exp\{\frac{(T'_n - T_n)T'_t}{(f\sigma_o/\sqrt{3} - T'_t)T'_n}\}) & \text{if } T_n > T'_n \end{cases} \ . \tag{8}$$

T_n and T_t are the normal and shear stresses along the interface, respectively. T_n' and T_t' are the values of T_n and T_t at the limit of proportionality. The friction factor, f, is a measure of the previously mentioned ratio of real contact area to apparent contact area. and its equivalence with the familiar coefficient of friction, μ, is made through the following expression due to Wanheim and Bay (1978):

$$\mu = \frac{f}{1 + \frac{\pi}{2} + \cos^{-1}(f) + \sqrt{1 - f^2}}.$$ (9)

The physical relevance of equation (8) is perhaps made more clear by a plot of its result. Figure 1 shows a plot of $|T_t|/\sigma_o$ vs. T_n/σ_o for various values of the friction factor f. Durham and Assempoor (1990) implemented both the Wanheim and Bay model and the Coulomb friction model into a finite element code. They modeled the plane-strain compression of a wedge-shaped specimen and found the Wanheim and Bay model to be in close proximity to experimentally determined loads and geometry. The frictional stresses predicted by the Coulomb model were unrealistically high.
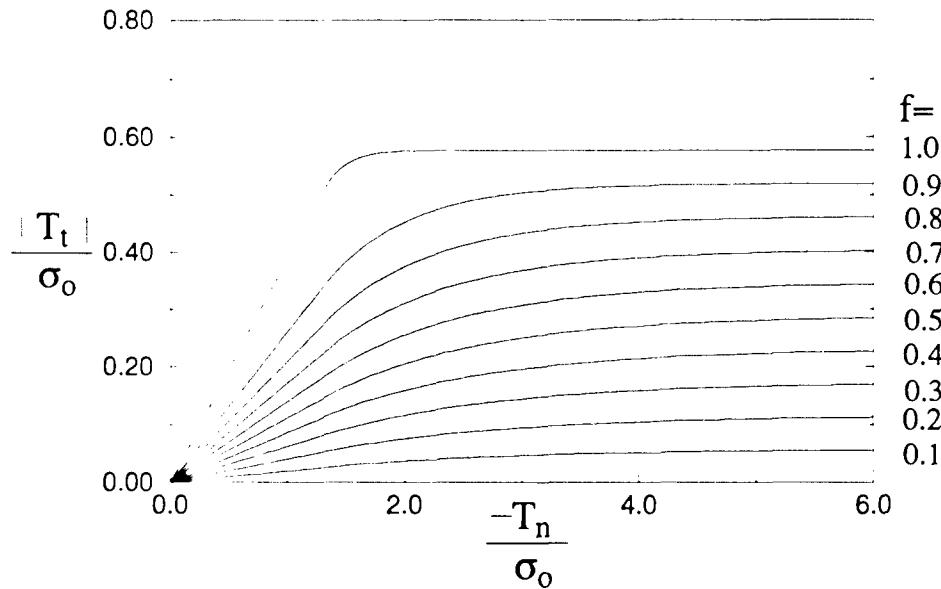
Figure 1. Plot of Wanheim and Bay's expression for friction as a function of normal stress.

2.3 Constitutive Modeling for the Finite Element Analysis

In order that the roll-gap displacement field be properly described, it is necessary to achieve at least a reasonable fit to the polycrystal aggregate behavior. Toward this end, we have implemented the temperature- and strain-rate-dependent plasticity model due to Bammann (1990).

6

In order to obtain an accurate description of global material behavior, Bammann (1990) has incorporated many microstructural features into a continuum model as they might behave in a statistical fashion. The model assumes that inelastic flow is dependent upon the current stress state and two internal variables, which are said to describe the statistical behavior of dislocation mechanics on a continuum level. The internal variables evolve in a hardening minus recovery format so as to account for both dislocation pile up and recovery due to cross slip. Further, this model can account for the rate sensitivity of both the yield stress and each recovery mechanism separately. The model develops as follows: when stresses are small in comparison to the elastic moduli, the elastic constitutive relation is specified by

$$\overset{\circ}{\boldsymbol{\sigma}} \approx \mathcal{L} : \mathbf{D^e}, \tag{10}$$

where the Cauchy stress, $\boldsymbol{\sigma}$, is convected with the elastic spin Ω^* as

$$\overset{\circ}{\boldsymbol{\sigma}} = \dot{\boldsymbol{\sigma}} - \Omega^* \cdot \boldsymbol{\sigma} + \boldsymbol{\sigma} \cdot \Omega^*, \tag{11}$$

and $\mathcal{L}$ is the fourth-order tensor of elastic moduli. Under the assumption of isotropic elasticity, equation (10) becomes

$$\overset{\circ}{\boldsymbol{\sigma}} = \lambda tr(\mathbf{D^e})\mathbf{1} + 2G\mathbf{D^e} . \tag{12}$$

The decomposition of the skew symmetric and symmetric parts of the velocity gradient is written as

$$\mathbf{D^*} = \mathbf{D} - \mathbf{D^P}, \tag{13}$$

and

$$\Omega^* = \Omega - \Omega^P, \tag{14}$$

where $\mathbf{D^*}$ and Ω^* represent the elastic part of the rate of deformation and the elastic spin, respectively.

To complete the constitutive description, assume $\mathbf{W^P} = 0$, thus recovering the Jaumann stress rate, and then define the flow rule as

$$\mathbf{D^P} = f(\theta)\sinh\left[\frac{|\boldsymbol{\xi}| - \kappa - Y(\theta)}{V(\theta)}\right]\frac{\boldsymbol{\xi}'}{|\boldsymbol{\xi}'|}, \tag{15}$$

where κ is the scalar hardening variable, θ represents temperature, and $\boldsymbol{\xi}'$ represents the translation of the yield surface with the back stress $\boldsymbol{\alpha}'$ as

$$\boldsymbol{\xi}' = \boldsymbol{\sigma}' - \boldsymbol{\alpha}' . \tag{16}$$

The temperature dependence of the scalar functions $f(\theta)$, $Y(\theta)$, and $V(\theta)$ is discussed later.

The evolution of the internal variables κ and $\boldsymbol{\alpha}$ is described as

$$\dot{\boldsymbol{\alpha}} = h(\theta)\mathbf{D^p} - [r_d(\theta)|\mathbf{D^p}| + r_s(\theta)]|\boldsymbol{\alpha}|\boldsymbol{\alpha}, \tag{17}$$

and

$$\dot{\kappa} = H(\theta)|\mathbf{D^p}| - [R_d(\theta)|\mathbf{D^p}| + R_s(\theta)]\kappa^2. \tag{18}$$

In this description. $h(\theta)$ and $H(\theta)$ represent standard hardening moduli with the exception that they depend on temperature. The scalar functions denoted by $r_s(\theta)$, $R_s(\theta)$, $r_d(\theta)$, and $R_d(\theta)$ represent the static and dynamic recovery terms respectively. These constants can be determined as in Schoenfeld et al. (1991), where the previously discussed model is calibrated to the aggregate polycrystal response of face-centered cubic (FCC) single crystals as described by the Asaro and Needleman (1985) polycrystal model. A general implementation of this model requires that the contact algorithm be aware of the flow stress in pure shear along the contact surface, a requirement greatly complicated by the anisotropic material description. In order to simplify this procedure, our implementation of the Wanheim friction model assumes isotropic material behavior and therefore requires only an approximation of the uniaxial tensile strength of the material. For the current analysis we neglect the kinematic terms in the material description. Even though such hardening is ideal in order to model bulk anisotropies due to large-strain textural hardening, such constitutive details will not be required for the finite element portion of our analysis. The material strength in uniaxial tension can be estimated from equation (15) by first substituting $\mathbf{D}$ for $\mathbf{D}^p$ (a reasonable approximation after the first few percent strain) and then inverting the expression to get

$$\sigma_0 = \sqrt{\frac{3}{2}} \left(\kappa - \beta(|\mathbf{D}|, \theta) \right), \tag{19}$$

where
$$\beta(|\mathbf{D}|, \theta) = Y(\theta) + V(\theta) \sinh^{-1} \left(\frac{|\mathbf{D}|}{f(\theta)} \right). \tag{20}$$

We use σ_0 to serve as our estimate for the material strength in uniaxial tension to be used in the calculation of frictional shears.

2.4   Finite Element Model

To model the workpiece, approximately 3,000 initially square, 4-node, plane-strain quadrilaterals are used with 11 elements through the thickness. Single gauss point integration, along with standard DYNA2D hourglass control (Hallquist 1982), is applied to each quadrilateral element. The workpiece is given a small initial velocity so as to bring it into contact with the roll where frictional conditions pull the piece through the roll gap.

The roll is modeled as an elastic annulus whose deformability would allow an accurate representation of the contact zone. Angular velocities are applied to the inner nodes, while the outer nodes are defined as the contact surface that will interact frictionally with the workpiece. The velocities of the inner nodes are prescribed throughout the entire calculation. Since the rolling process is symmetric, the appropriate boundary conditions are applied at the center of the rolled workpiece. In following with the notation of Truszkowski, Krol, and Major (1980) and Truszkowski and Kiel (1982), we will refer to position through the thickness of the workpiece by the parameter $S = 2\Delta x/h$, where Δx is the distance from the sheet center, and h is the thickness of the sheet. Thus, $S = 1$ refers to the sheet surface, while $S = 0$ refers to the sheet center. During a finite element calculation, a position is picked along

8

the workpiece such that it is far enough away from either end that it will undergo steady-state rolling conditions. At this location along the workpiece, three elements are chosen whose gauss points are at $S = 0.05, 0.5$, and 0.95, and the displacement time histories for the nodes composing each element are then saved for use in a polycrystal averaging scheme.

Since two different roll gaps are to be modeled, the model is changed only by scaling the dimensions of the workpiece. The roll itself and the reduction in thickness are held constant. An example of the deformed mesh for one of the test cases is shown in Figure 2. This figure has fewer elements through the cross section and shows the deformation state of each element more clearly.
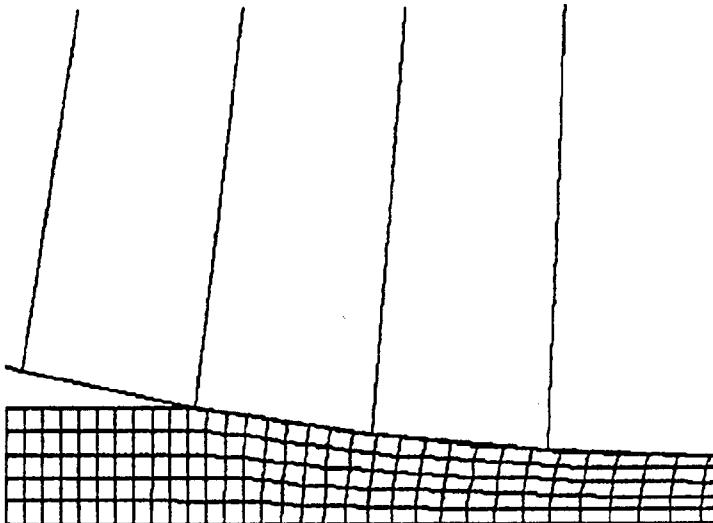
Figure 2. Deformed finite element mesh with large draught rolling.

3. Texture Analysis

In the analysis that follows the calculation of the roll-gap displacement field, the polycrystal textural response is calculated through the use of the detailed rate-dependent constitutive model of Asaro and Needleman (1985). In this model, attention is paid to the elastic-viscoplastic behavior of an initially random distribution of single crystals. The individual crystal responses are then averaged to give a macroscopic aggregate behavior.

The constitutive description begins with the response of single crystals. Important single-crystal microstructural aspects are incorporated into a continuum framework so as to simulate the complex micromechanics of single crystals. For the present purposes, an isothermal version of the theory will suffice.

The kinematics of single-crystal deformation are as follows. The material is allowed to flow

through the lattice due to dislocation motion, and then the lattice, with material embedded in it. is subjected to elastic deformations and rigid rotations. For the isothermal deformations considered here. the deformation gradient, $\mathbf{F}$, is decomposed as

$$\mathbf{F} = \mathbf{F}^* \cdot \mathbf{F}^p, \tag{21}$$

where

$$\mathbf{F} \equiv \frac{\partial \mathbf{x}}{\partial \mathbf{X}}, \tag{22}$$

with $\mathbf{x}$ and $\mathbf{X}$ denoting the current and reference configuration of the material.

The deformations due to $\mathbf{F}^p$ represent path-dependent strain on the crystallographic slip systems. while the deformations in $\mathbf{F}^*$ represent the elastic stretching and rotations of the lattice.

A particular slip system is denoted by α and defined by a slip plane normal, $\mathbf{m}^{(\alpha)}$, and slip direction. $\mathbf{s}^{(\alpha)}$, which are taken as initially orthogonal in the undeformed configuration and allowed to convect with the lattice so as to become

$$\mathbf{s}^{*(\alpha)} = \mathbf{F}^* \cdot \mathbf{s}^{(\alpha)}, \tag{23}$$

and

$$\mathbf{m}^{*(\alpha)} = \mathbf{m}^{(\alpha)} \cdot \mathbf{F}^{*-1}. \tag{24}$$

These definitions have been shown to give a precise statement of normality in terms of work conjugate measures of stress and strain when the rate is taken to be only a function of the so-called resolved shear stress defined later. Collectively, equations (21) through (24) define the plastic part of the rate of stretching tensor, $\dot{\mathbf{F}} \cdot \mathbf{F}^{-1}$, as

$$\dot{\mathbf{F}} \cdot \mathbf{F}^{-1} - \dot{\mathbf{F}}^* \cdot \mathbf{F}^{*-1} = \mathbf{D}^p + \mathbf{\Omega}^p = \sum_\alpha \mathbf{s}^{*(\alpha)} \mathbf{m}^{*(\alpha)} \dot{\gamma}^{(\alpha)}, \tag{25}$$

where $\dot{\gamma}^{(\alpha)}$ denotes the rate of shearing on each slip system α, and summation is carried out over all slip systems.

For notational convenience, the symmetric and antisymmetric tensors on each slip system are defined. respectively, as,

$$\mathbf{P}^{(\alpha)} = \frac{1}{2}[\mathbf{s}^{*(\alpha)} \mathbf{m}^{*(\alpha)} + \mathbf{s}^{*(\alpha)} \mathbf{m}^{*(\alpha)}], \tag{26}$$

and

$$\mathbf{W}^{(\alpha)} = \frac{1}{2}[\mathbf{s}^{*(\alpha)} \mathbf{m}^{*(\alpha)} - \mathbf{s}^{*(\alpha)} \mathbf{m}^{*(\alpha)}], \tag{27}$$

so that now we can express the plastic parts of the rate of stretching and the spin tensors, respectively, as,

$$\mathbf{D}^p = \sum_\alpha \mathbf{P}^{(\alpha)} \dot{\gamma}^{(\alpha)}, \tag{28}$$

and

$$\mathbf{\Omega}^P = \sum_\alpha \mathbf{W}^{(\alpha)} \dot{\gamma}^{(\alpha)}. \tag{29}$$

10

Their elastic counterparts, $\mathbf{D}^*$ and $\boldsymbol{\Omega}^*$, are simply the symmetric and antisymmetric parts of $\dot{\mathbf{F}}^* \cdot \mathbf{F}^{*-1}$, which entirely contain the lattice deformation and rigid-body rotations.

The elasticity of the single crystal is said to be characterized by a strain energy function Φ that is defined only for processes exclusively involving elastic strain. The work increment per unit reference volume done by such a deformation would then be

$$\delta W = \boldsymbol{\tau} : \delta \mathbf{F}^* \cdot \mathbf{F}^{*-1} = \delta \Phi, \tag{30}$$

which allows the rate form

$$\dot{W} = \boldsymbol{\tau} : \dot{\mathbf{F}}^* \cdot \mathbf{F}^{*-1} = \dot{\Phi}. \tag{31}$$

Note that $\boldsymbol{\tau}$ is the Kirchhoff stress that is related to $\boldsymbol{\sigma}$, the Cauchy stress as $\boldsymbol{\tau} \equiv \det(\mathbf{F})\boldsymbol{\sigma} = (\rho_0/\rho)\boldsymbol{\sigma}$ with ρ and ρ_0 as the densities in the deformed and undeformed states.

Allowing $\mathbf{S}^*$ and $\mathbf{E}^*$ to denote conjugate stress and strain measures, we can rewrite equation (30) as

$$\delta W = \mathbf{S}^* : \delta \mathbf{E}^* = \delta \Phi(\mathbf{E}^*), \tag{32}$$

from which

$$\mathbf{S}^* = \frac{\partial \Phi}{\partial \mathbf{E}^*}, \tag{33}$$

and, by the chain rule,

$$\dot{\mathbf{S}}^* = \frac{\partial^2 \Phi}{\partial \mathbf{E}^* \partial \mathbf{E}^*} : \dot{\mathbf{E}}^*. \tag{34}$$

Taking $\mathbf{E}^*$ to be the lattice Green strain as in Hill and Havner (1975) defined by

$$\mathbf{E}^* = \frac{1}{2}[\mathbf{F}^{*T} \cdot \mathbf{F}^* - \mathbf{I}], \tag{35}$$

then

$$\boldsymbol{\tau} = \mathbf{F}^* \cdot \mathbf{S}^* \cdot \mathbf{F}^{*T}, \tag{36}$$

or

$$\boldsymbol{\tau} = \mathbf{F}^* \cdot \frac{\partial \Phi}{\partial \mathbf{E}} \cdot \mathbf{F}^{*T}, \tag{37}$$

which can now be differentiated with respect to time to yield

$$\overset{\triangledown}{\boldsymbol{\tau}}{}^* = \dot{\boldsymbol{\tau}} - \boldsymbol{\Omega}^* \cdot \boldsymbol{\tau} + \boldsymbol{\tau} \cdot \boldsymbol{\Omega}^* = \mathbf{L}^* : \mathbf{D}^* + \mathbf{D}^* \cdot \boldsymbol{\tau} + \boldsymbol{\tau} \cdot \mathbf{D}^*, \tag{38}$$

where $\overset{\triangledown}{\boldsymbol{\tau}}$ is the Jaumann rate of Kirchhoff stress formed on axes that spin with the lattice, and $\mathbf{L}^*$ is defined as

$$\mathbf{L}^* = \mathbf{F}^* \cdot \mathbf{F}^* \frac{\partial^2 \Phi}{\partial \mathbf{E}^* \partial \mathbf{E}^*} \cdot \mathbf{F}^{*T} \cdot \mathbf{F}^{*T}. \tag{39}$$

At this point, it is quite common in the implementation of metal elastic-plastic laws to introduce two assumptions. First, as long as the magnitudes of the stresses are small compared to the elastic moduli, the last two terms in $\mathbf{D}^*$ of equation (38) are neglected. Second, the components of $\mathbf{L}^*$ are taken equal to their reference state values. These assumptions are carried through the rest of the discussion and will be the only assumptions required in the complete

description of material or stress rotations. It is still necessary to describe the flow and strain hardening that occur on the crystallographic slip systems. This will be accomplished within the framework of a Schmid-like rule.

The constitutive law will now be phrased in terms of the stress rates formed on material axes. The relation between the Jaumann stress rate formed on axes that spin with the material and the lattice is found from the purely kinematical relations (equations (28) and (29)) as

$$\overset{\triangledown}{\tau}^* = \overset{\triangledown}{\tau} + \sum \beta^{(\alpha)} \dot{\gamma}^{(\alpha)}, \tag{40}$$

where

$$\beta^{(\alpha)} = \mathbf{W}^{(\alpha)} \cdot \tau - \tau \cdot \mathbf{W}^{(\alpha)}. \tag{41}$$

From equations (38) and (40), this becomes

$$\overset{\triangledown}{\tau} = \mathbf{L} : \mathbf{D} - \sum_\alpha \mathbf{R}^{(\alpha)} \dot{\gamma}^{(\alpha)}, \tag{42}$$

where

$$\mathbf{R}^{(\alpha)} = \mathbf{L} : \mathbf{P}^{(\alpha)} + \beta^{(\alpha)}. \tag{43}$$

Now with a simple adaptation of the Schmid rule of critical resolved shear stress, we can complete the constitutive law with a relationship between $\dot{\gamma}^{(\alpha)}$ and the current stress and material state. This is specified in the form of

$$\dot{\gamma}^{(\alpha)} = \dot{a}^{(\alpha)} \left[\frac{\tau^{(\alpha)}}{g^{(\alpha)}} \right] \left[\left| \frac{\tau^{(\alpha)}}{g^{(\alpha)}} \right| \right]^{\frac{1}{(m)} - 1}, \tag{44}$$

where $\dot{a}^{(\alpha)}$ is a reference rate of shearing, such that if $\tau^{(\alpha)} = g^{(\alpha)}$, then $\dot{a}^{(\alpha)}$ is the resulting rate of shear. The slip system's strength and strain hardening are described by the hardening law

$$\dot{g}^{(\alpha)} = \sum_\beta h_{\alpha\beta} |\dot{\gamma}^{(\beta)}|. \tag{45}$$

Note that the absolute magnitude in this equation rules out Bauschinger effects on individual slip systems, but this could easily be modified.

Polycrystal averaging is achieved in an approximate fashion that ensures compatibility is satisfied between each grain. Equilibrium, which is satisfied within each grain, may be violated in between individual grains. Asaro and Needleman (1985) pose the single-crystal constitutive (equation [42]) in the form

$$\dot{\mathbf{n}} = \mathbf{K} : \dot{\mathbf{F}} - \dot{\mathbf{B}}, \tag{46}$$

by relating the nominal stress, $\mathbf{n}$, to the Kirchoff stress, τ, through

$$\mathbf{n} = \mathbf{F}^{-1} \cdot \tau. \tag{47}$$

Taking the average of equation (46), we obtain

$$\langle \dot{\mathbf{n}} \rangle = \langle \mathbf{K} \colon \dot{\mathbf{F}} - \dot{\mathbf{B}} \rangle, \tag{48}$$

and

$$\langle \dot{\mathbf{n}} \rangle = \langle \mathbf{K} \colon \dot{\mathbf{F}} \rangle - \langle \dot{\mathbf{B}} \rangle. \tag{49}$$

Compatibility is ensured by the assumption that each grain undergoes the same deformation as the macroscopic aggregate; thus, equation (49) simplifies to

$$\langle \dot{\mathbf{n}} \rangle = \langle \mathbf{K} \rangle \colon \dot{\mathbf{F}} - \langle \dot{\mathbf{B}} \rangle. \tag{50}$$

Assuming that the volume fractions of each grain are identical, the macroscopic constitutive law becomes

$$\dot{\overline{\mathbf{n}}} = \overline{\mathbf{K}} \colon \dot{\mathbf{F}} - \dot{\overline{\mathbf{B}}}, \tag{51}$$

where

$$\dot{\overline{\mathbf{n}}} = \frac{1}{N} \sum_{i=1}^{N} \dot{\mathbf{n}}^{(i)}, \tag{52}$$

$$\overline{\mathbf{K}} = \frac{1}{N} \sum_{i=1}^{N} \mathbf{K}^{(i)}, \tag{53}$$

and

$$\dot{\overline{\mathbf{B}}} = \frac{1}{N} \sum_{i=1}^{N} \dot{\mathbf{B}}^{(i)}, \tag{54}$$

where N is the total number of grains, and the superscript i refers to the i*th* grain, thus implying macroscopic equilibrium, Hill and Havner (1975).

4. Results

The preceding analysis was done in two phases. First, the roll-gap displacement field was calculated by a finite element analysis. Second, the displacement time histories were used as the macroscopic boundary conditions for the calculation of polycrystal texture at points of interest through the thickness of the workpiece. The success of our analysis depends on the fact that specific macroscopic constitutive features should have little effect on the actual through-thickness displacement fields. Such fields will be highly constrained and, as such, will be dependent on the macroscopic boundary conditions and relatively insensitive to material hardening. Toward this end, the hardening form of the single-crystal material description was chosen to be

$$h_{\alpha\beta} = h_0 \mathrm{sech}^2 \left(\frac{h_0 \gamma^\beta}{\tau_s - \tau_0} \right), \tag{55}$$

where h_0 represents the initial hardening rate, and τ_0 and τ_s represent the initial and saturation resistance to slip, respectively. This functional form for the single-crystal hardening

law provides for the simulation of a wide variety of strain hardening behavior. In the current study, strain rate sensitivity was minimized by taking $m = 0.005$, and strain hardening in the single crystals was scaled so that $h_0 = 8.9\tau_0$ and $\tau_s = 1.8\tau_0$. This is a rapidly saturating functional form of the strain hardening law chosen only for convenience. It may be said to reflect the late strain hardening in heavily work-hardened aluminum sheet (representative of the final rolling passes), or it may only be a naive statement of material behavior. In either case, it will function within our analysis as a stable work-hardening material description useful in order to resolve the roll-gap displacement field. The elastic constants chosen reflect the cubic symmetry of aluminum single crystals, specifically, $c_{11} = 1070\tau_0$, $c_{12} = 608\tau_0$, and $c_{44} = 283\tau_0$. Specification of the single crystal elastic and strain hardening terms determines the macroscopic behavior of the polycrystal. This is shown in Figure 3 along with our best fit to polycrystal data using Bammann's model. In fitting to Bammann's model, both the thermal and anisotropic behavior of the material have been neglected. Thus, all functions of temperature reduce to constants, while variables describing the kinematic hardening tensor α become zero. The fitted values are given as $Y = 3.01\tau_0$, $f = 1.0$, $R_s = 13\tau_0$, and $R_d = 80\tau_0$. The elastic constants used in Bamman's model are the corresponding macroscopic averaged crystal quantities using the initially random distribution of single crystals. They are given here as $\lambda = 658.46\tau_0$ and $G = 263.0\tau_0$. It should again be noted that this is only a simple and convenient material description, and that actual stresses within the material during processing are not of interest to the current study. The rolls were modeled as isotropically elastic with a Young's modulus of $3000\tau_0$ and a Poisson's ratio of $1/3$.
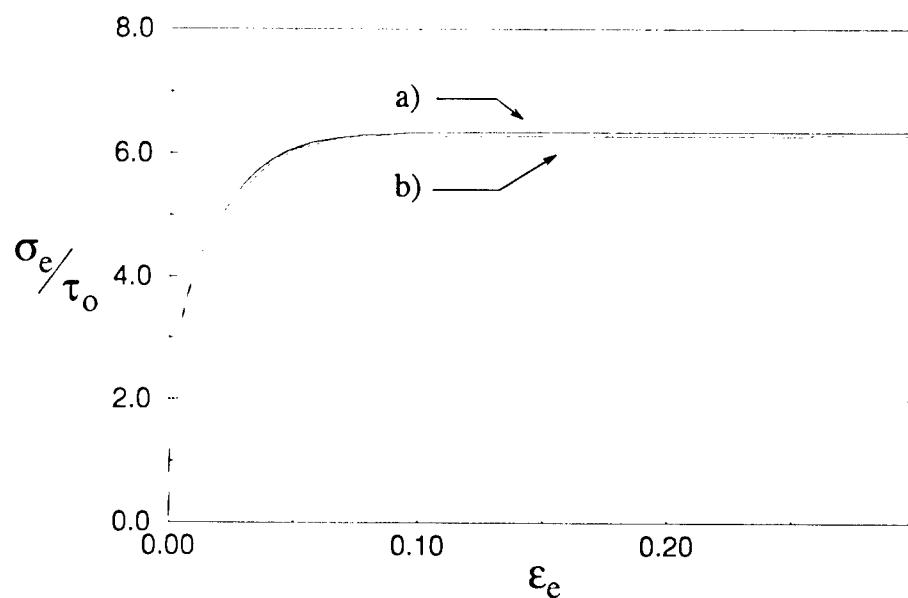

Figure 3. Normalized effective stress vs. effective strain curves: (a) constitutive model used in FEM and (b) macroscopic polycrystal aggregate behavior.

In the analysis that follows, two different roll-gap geometries are discussed. The first one is referred to as large draught rolling and maintains the ratio $l_c/h = 5.0$. This corresponds to a 40% reduction in thickness per pass under the rolls. The second roll-gap geometry is referred to as small draught rolling, thus maintaining the ratio $l_c/h = 0.5$, or a reduction of 4% in thickness per pass. These two particular roll gaps are important as they are representative of roll gaps that produce two distinctly different through-thickness deformation fields (Truszkowski, Krol and Major 1980). Most roll gaps encountered during rolling have one or the other or a hybrid of these two types of through-thickness deformation fields. Before discussing texture results, it is of interest to examine the roll-gap displacement field in some detail.

4.1 Roll-Gap Displacement Field

As an element of material is compressed in the roll gap, it also lengthens in the rolling direction. This causes the velocity of the workpiece to increase during the rolling process. It would stand to reason that at some point in the roll gap, the roll and workpiece move with the same velocity. This is the neutral point. As an element at the surface of the workpiece passes under the roll, it is first sheared in one direction as its velocity is less than the roll and then sheared in the reverse direction after it passes the neutral point and attains a velocity greater than the roll. Figure 4(a) is a plot of frictional shear stress normalized by the flow stress in simple shear vs. the distance along the contact length normalized by the length of contact for the large draught model with $\mu = 0.2$. As an element comes into contact with the roll, its relative velocity is slower than the roll, and sliding friction will work to accelerate the element. As the velocity of the element approaches that of the roll, shear stresses drop as full sticking occurs at the neutral point. As the element passes the neutral point, shear stresses are reversed as the material moves faster than the roll. In Figure 4(b), the frictional stress normalized by the material flow stress in simple shear is plotted along the interface for the case of small draught rolling with $\mu = 0.2$. For this case, the neutral point is located at the exit point in the roll gap. This suggests that the velocity of the workpiece never exceeds that of the roll, and that the applied surface tractions will be unidirectional. Figure 4 suggests that the relative position of the neutral point may be a function of roll-gap geometry. This point is further investigated in section 5 and shown to be only an anomaly of the particular roll gaps and coefficients of friction that were analyzed.

Figure 5 shows plots of compressive-strain time history. Figures 5(a) and (b) show large draught rolling with $\mu = 0.2$ and $\mu = 0.3$, respectively. Figure 5(c) is for small draught rolling with $\mu = 0.2$. In Figure 5 it can be seen that compressive-strain time histories are not homogeneous throughout the roll gap, but converge by the end of the rolling process to approximately the average compressive strain due to the final macroscopic reduction in thickness, ϵ_{22}^f. Figure 6(a) is a plot of shear strain, ϵ_{12}, normalized by $|\epsilon_{22}^f|$, vs. time (normalized by the total time for an element of material to pass through the roll gap) for three through-thickness positions during a single pass of large draught rolling with $\mu = 0.2$. Figure 6(b) shows the same roll-gap geometry with $\mu = 0.3$. Comparing Figures 6(a) and (b), we can see that larger surface shear strains were achieved as well as higher shear strains
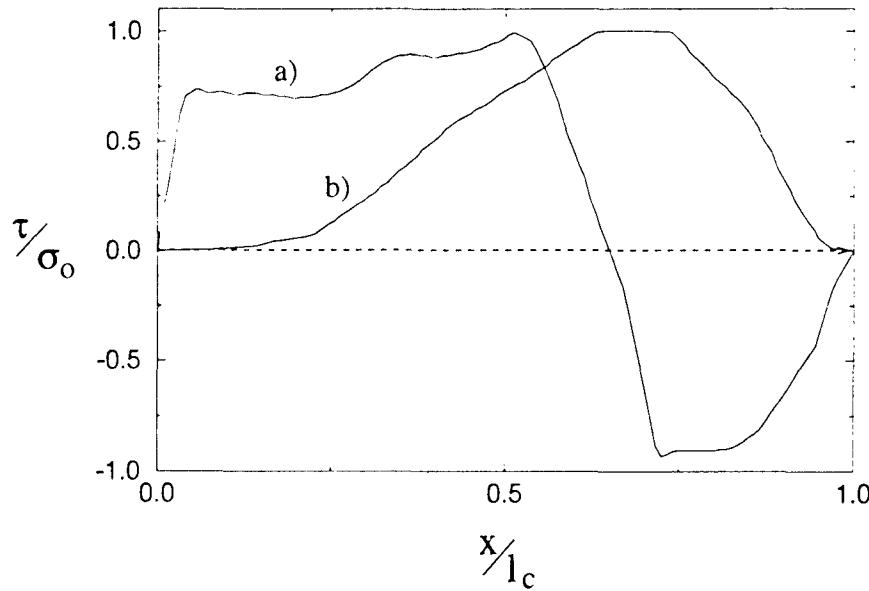
Figure 4. Interface shear stress normalized by material flow stress in simple shear vs. distance along the interface normalized by the length of the interface for (a) large draught rolling with $\mu = 0.2$ and (b) small draught rolling with $\mu = 0.2$.

in the intermediate layer. Figure 6(c) is the shear-strain time history for the small draught rolling with $\mu = 0.2$. Note here that the surface shear strain is not as high as in the large draught rolling. One factor contributing to this phenomenon is that normal pressures do not develop in small draught rolling to the same extent as in large draught rolling. A more likely reason that surface shearing is less in the small draught case, is that the contact length is much smaller than in the large draught case and there is not enough time for large shears to develop, especially when, as previously mentioned, full sticking never actually develops. What is interesting is that the intermediate layer at $S = 0.5$ develops a reversed shearing with respect to the surface-layer shear. A possible explanation of this is given in section 5.

4.2 Texture Calculations

The three roll-gap displacement fields calculated in the previous section were used in calculations to resolve textures through the thickness of each workpiece. In order for the overall roll-gap geometry to be preserved, multiple passes were modeled as repeated application of the single-pass deformation-gradient time history. Therefore, repeated finite element calculations were not necessary. For materials that continue to harden past the first few percent strain. this approach may not be applicable because material properties continue to vary with each pass through the roll gap. Referring to Figure 3, we see that our particular material model saturates rapidly, and that the material state will remain relatively constant with each pass. In order to verify that this is the case, the large draught displacement

16
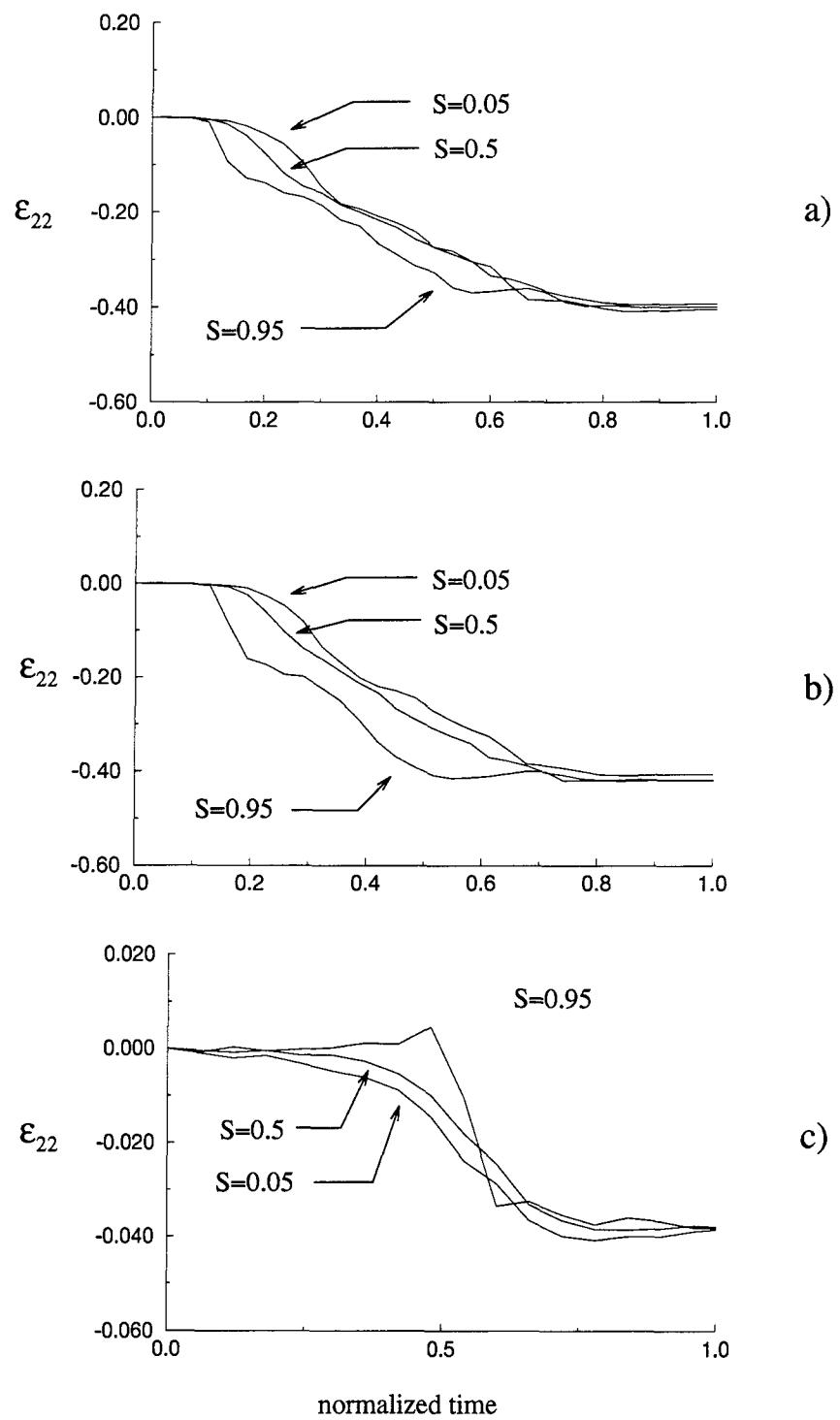
Figure 5. Compressive-strain time history for (a) large draught rolling with $\mu = 0.2$, (b) large draught rolling with $\mu = 0.3$, and (c) small draught rolling with $\mu = 0.2$.
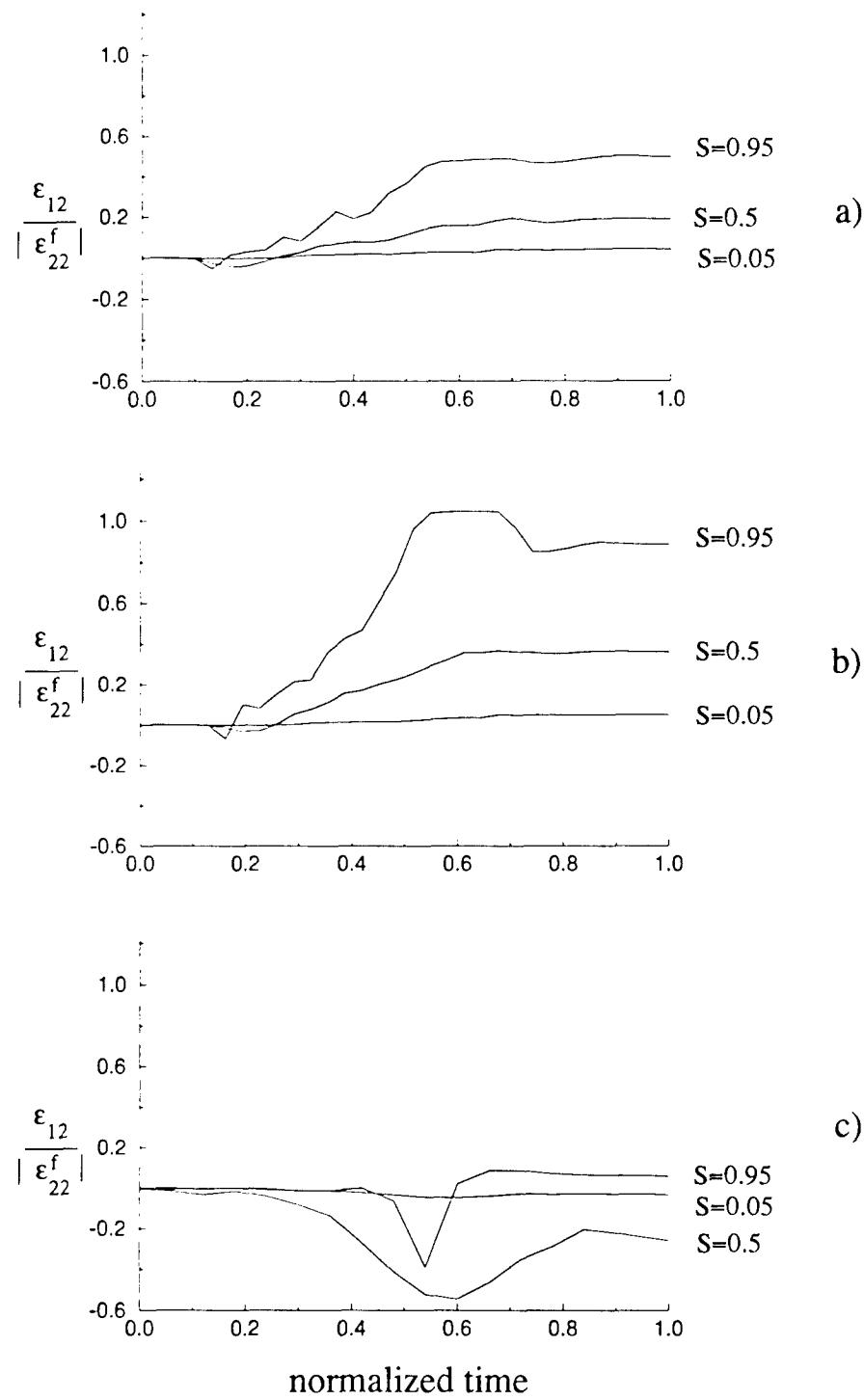
Figure 6. Shear-strain time history for (a) large draught rolling with $\mu = 0.2$, (b) large draught rolling with $\mu = 0.3$, and (c) small draught rolling with $\mu = 0.2$.

18

field was recalculated using the material state from the original finite element calculation. The shear-strain time history for the second pass calculated by restarting the finite element model is shown in Figure 7. With the exception of the roll-gap entrance, the final strain state at the end of the rolling process is quite representative of any particular pass, and this can be verified by comparison of Figure 7 to Figure 6(a). The advantage here is not just savings in computational effort, but also avoiding the mistake of many investigators who fail to maintain a constant roll-gap geometry. Often, in the literature, we find investigators who wish to investigate constant roll-gap effects, but proceed by maintaining constant thickness reduction. Since the overall roll-gap geometry is not preserved, small draught rolling becomes large draught rolling after several passes.
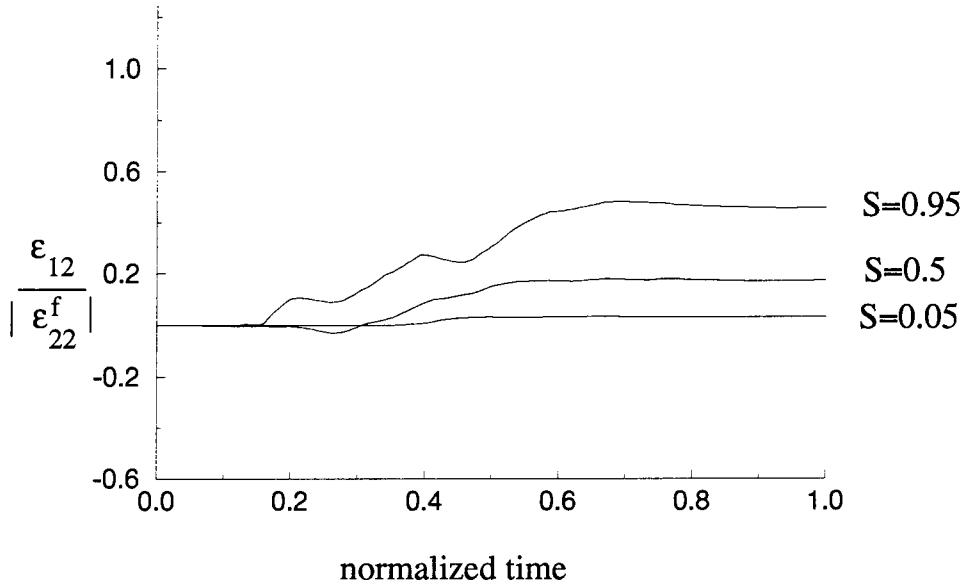

Figure 7. Shear-strain time history for a second pass of large draught rolling with $\mu = 0.2$.

For large draught rolling, an overall thickness reduction of 64% was obtained by two applications of the deformation-gradient time history (i.e., two passes at a reduction of 40% each pass) and an overall reduction of 87% was achieved by four passes. During small draught rolling, passes were made by reducing the thickness 4% each pass. Thus, 25 passes were required to reach 64% reduction, and 50 passes were required to reach 87% reduction.

Figure 8 shows {111} equal-area pole figures in the rolling direction/transverse direction plane for large draught rolling with $\mu = 0.2$. The texture shown in Figure 8(a) is for a reduction of 64%, while the texture in 8(b) is for a reduction of 87%.

The texture at S = 0.05 is the well-known plane-strain compression Taylor model texture composed of mainly (110)[112] and (112)[111] ideal orientations. As we proceed upward toward the surface to S = 0.95, we see a rotation of the texture about the transverse direction, as is evident by the increasing significance of the (111)[112] and (100)[011] ideal orientations.

S=0.95

S=0.5

S=0.05

a)   b)
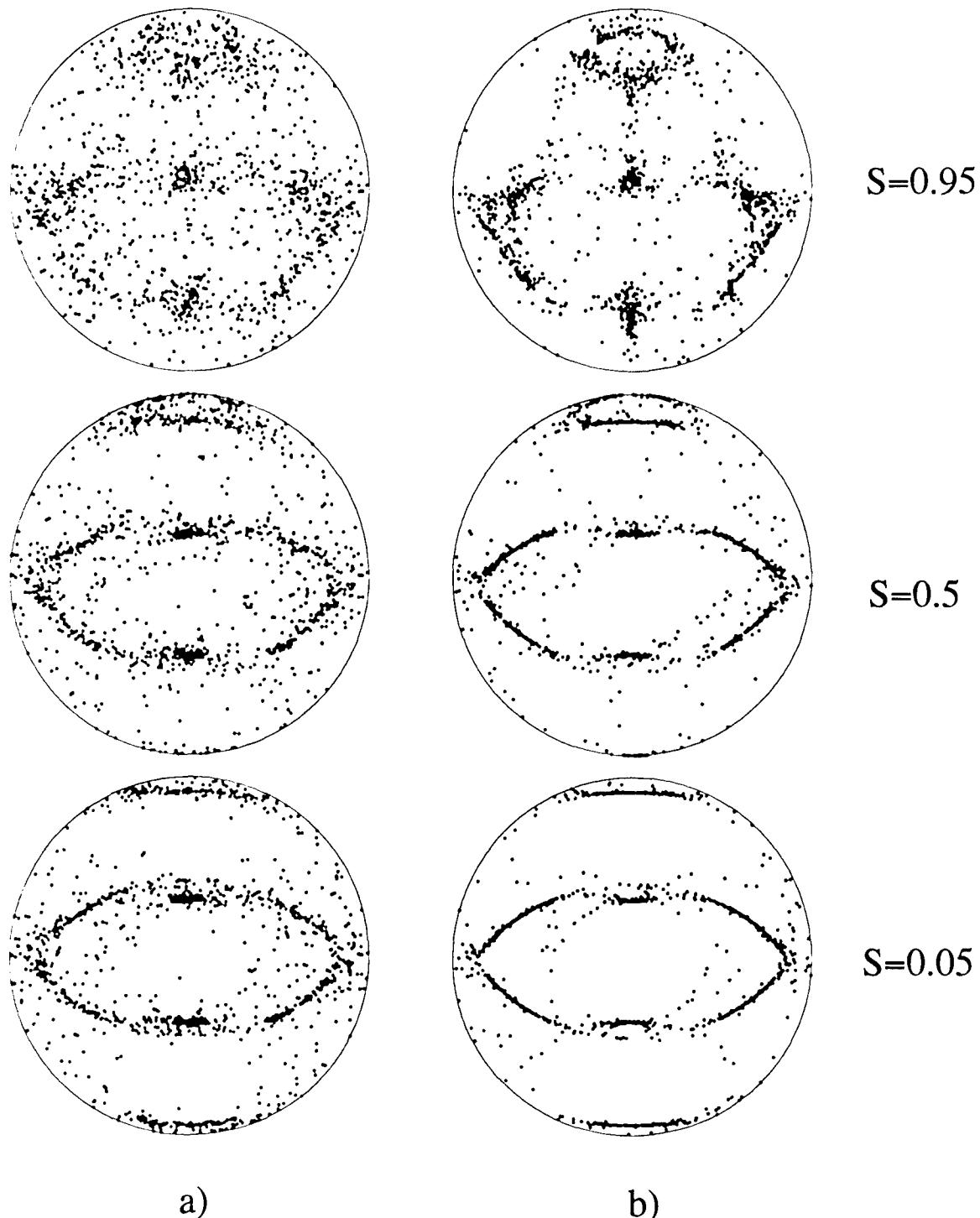
Figure 8. {111} equal-area pole figures for (a) 64% reduction and (b) 87% reduction by large draught rolling with $\mu = 0.2$.

20

Figures 9(a) and (b) corresponds to large draught rolling with $\mu = 0.3$. Recall from the previous section that the higher coefficient of friction created larger shear strains at the surface and deeper penetration of shear into the cross section. We can see these phenomena reflected in the relative sharper S = 0.95 and S = 0.5 textures of the $\mu = 0.3$ case. Also note that for $\mu = 0.3$, the texture has a slightly greater rotation about the transverse direction.

Figures 10(a) and (b) contain textures for small draught rolling with $\mu = 0.2$. Note that the near-surface textures are similar to the those of the large draught rolling with comparable friction. If we compare the S = 0.95 and S = 0.5 textures, we can see opposite rotations about the transverse direction as compared to the S = 0.05 texture. This observation is consistent with the shear time history plots of Figure 6.

Since textures have profound effects on subsequent material behavior, roll gap should be a consideration when designing a rolling procedure as part of a manufacturing process. In order to emphasize the macroscopic effects of roll-gap geometry on a final product, textured aggregates calculated from the rolling process have been reloaded to calculate yield surfaces as was done by Asaro and Needleman (1985). Both displacement and stress-type boundary conditions were applied in order to probe the tensile stress space in the plane of the rolled sheet. Since rolling was achieved by compression in the x_2 direction, this would be assumed to remain traction free, i.e.,

$$\dot{N}_{22} = \dot{N}_{21} = \dot{N}_{23} = 0. \tag{56}$$

Further, it was assumed that planes perpendicular to the compression, rolling, or transverse directions maintained their orientations. Therefore,

$$\dot{f}_{12} = \dot{f}_{32} = \dot{f}_{13} = \dot{f}_{31} = 0. \tag{57}$$

Loading was achieved by prescribing $\dot{f}_{33}$ and then prescribing that normal stresses in the rolling plane remained proportional,

$$\dot{N}_{11} = c\dot{N}_{33}. \tag{58}$$

Since loading taken to occur from the previously deformed configuration

$$\mathbf{f} = \mathbf{F} \cdot \mathbf{F}_i^{-1}, \tag{59}$$

and

$$\mathbf{N} = \left(\frac{\mathbf{F}_i \cdot \mathbf{n}}{det(\mathbf{F}_i)} \right), \tag{60}$$

where $\mathbf{F}_i$ is the deformation gradient from the initial state to the final rolled state. By varying c and keeping track of the Mises effective plastic strain, surfaces of constant offset effective plastic strain equal to 0.005 were calculated. For plotting purposes, an interpolation scheme to find the 0.005 offset effective plastic strain was used. The calculations were very sensitive to this scheme and, as a result, any apparent loss of convexity in the results is simply an effect of the numerics.

Figure 11 shows three of these surfaces through the thickness of a large draught rolling specimen. The reference Mises ellipse is calculated by using the plane-strain Taylor factor

S=0.95

S=0.5

S=0.05

a)   b)
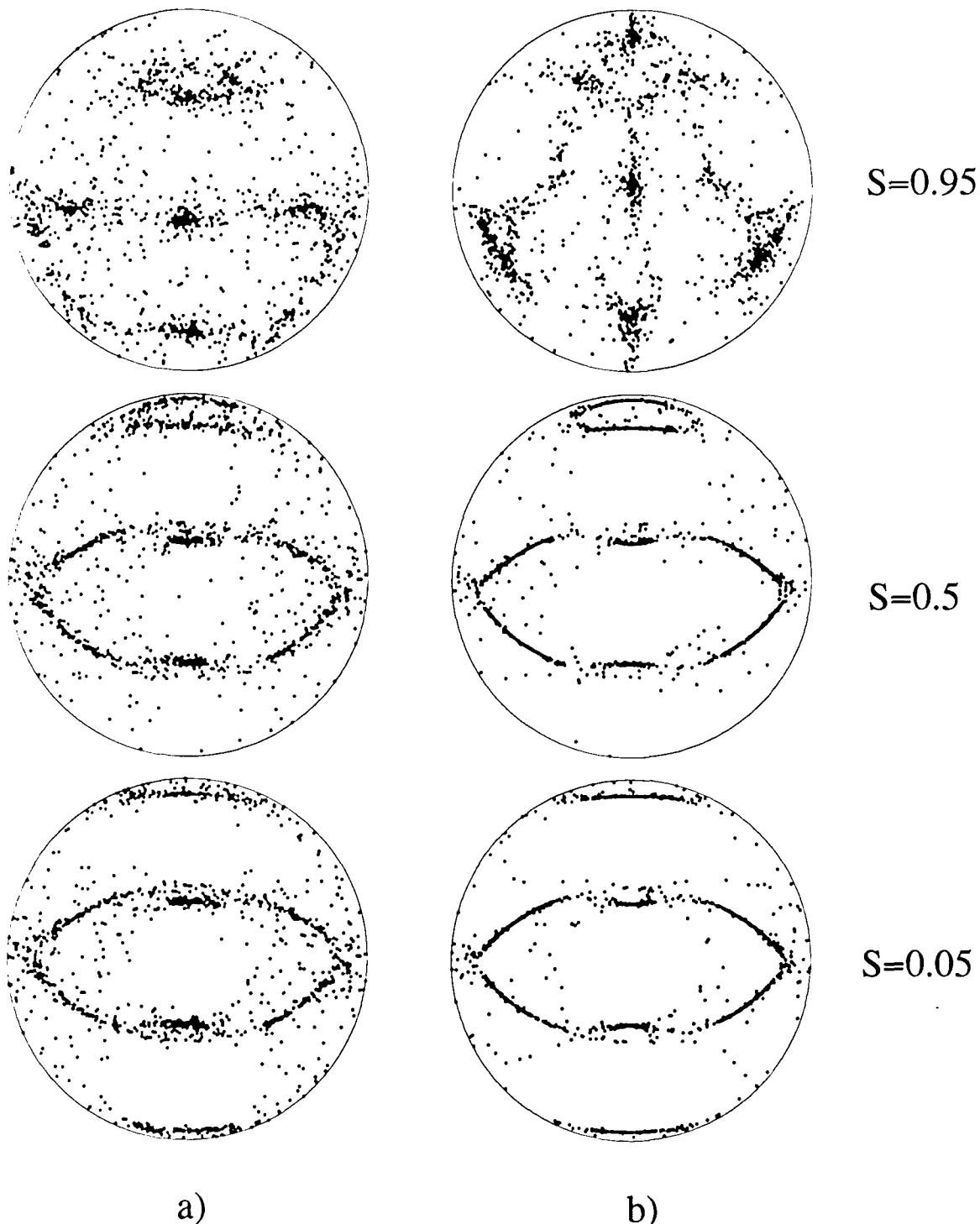
Figure 9. {111} equal-area pole figures for (a) 64% reduction and (b) 87% reduction by large draught rolling with $\mu = 0.3$.

S=0.95

S=0.5

S=0.05

a)   b)
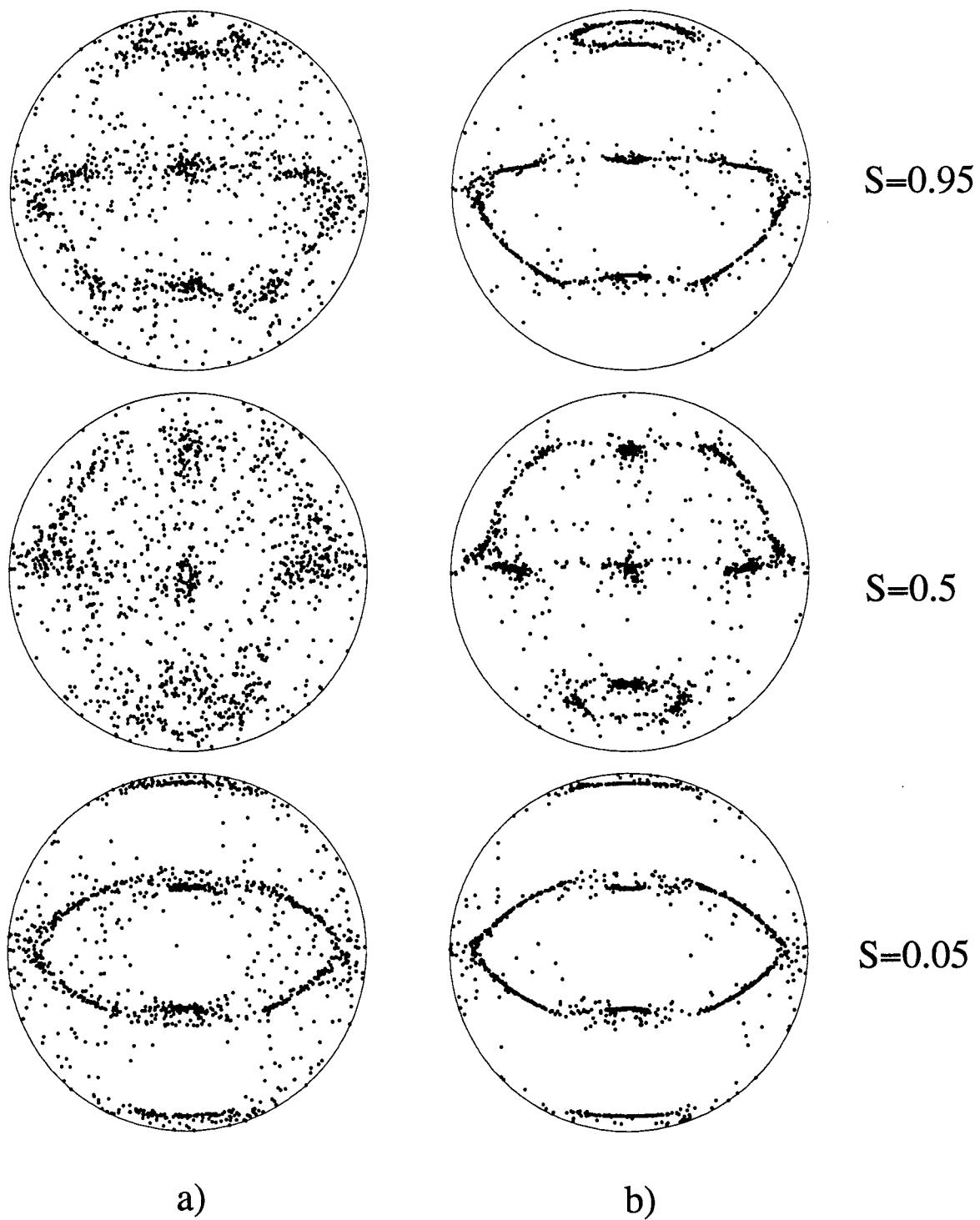
Figure 10. {111} equal-area pole figures for (a) 64% reduction and (b) 87%
reduction by small draught rolling and $\mu = 0.2$.

of $2.86 \times 1.8\tau_o$. Figure 12 shows the same through-thickness positions as Figure 11, but for small draught rolling with the same thickness reduction and frictional conditions. Note that yield surfaces vary more drastically through the thickness of the small draught case, and that even a comparison between yield surfaces at the center of each specimen show different behavior.
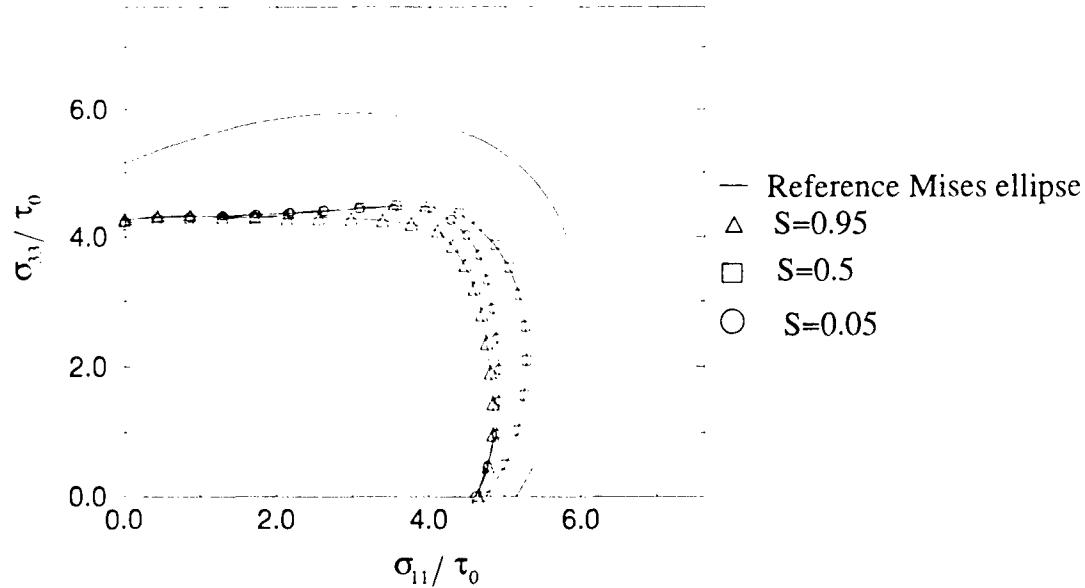

Figure 11. **Constant offset effective plastic strain yield surfaces through the thickness due to 65% thickness reduction by large draught rolling with** $\mu = 0.2$.

5. Discussion and Conclusions

Dillamore and Roberts (1963) cold-rolled commercial-purity aluminum to an overall reduction of 92%. They did this with constant reductions in thickness. Although they did not maintain a constant roll-gap geometry, the final passes were well within the large gap category. They estimated that the coefficient of friction between the rolls and workpiece was 0.2 and obtained {111} pole figures through the thickness for the final rolled product. These pole figures are shown in Figure 13(a) as solid lines superimposed on the calculated data of Figure 8(b). In Figure 13(a), we see that the calculated peaks correspond to within a few degrees of the experimental contours signifying the same rotation of texture about the transverse direction. In the calculation, there is a split in the top peak at the sheet surface that is not found in the experiment, while the experimental peak at the sheet center seems to be off by about $5°$ from the ideal (112)[111] orientation. Truszkowski, Krol, and Major (1980) also cold-rolled aluminum, which they reported as 99.5% by weight pure, and their results for 87.6% reduction are shown as solid lines in Figure 13(b) with the calculated data of Figure 8(b), again shown as discreet points. Here, we see excellent correspondence between the calculation and experiment for the location of surface peaks. The calculated

24
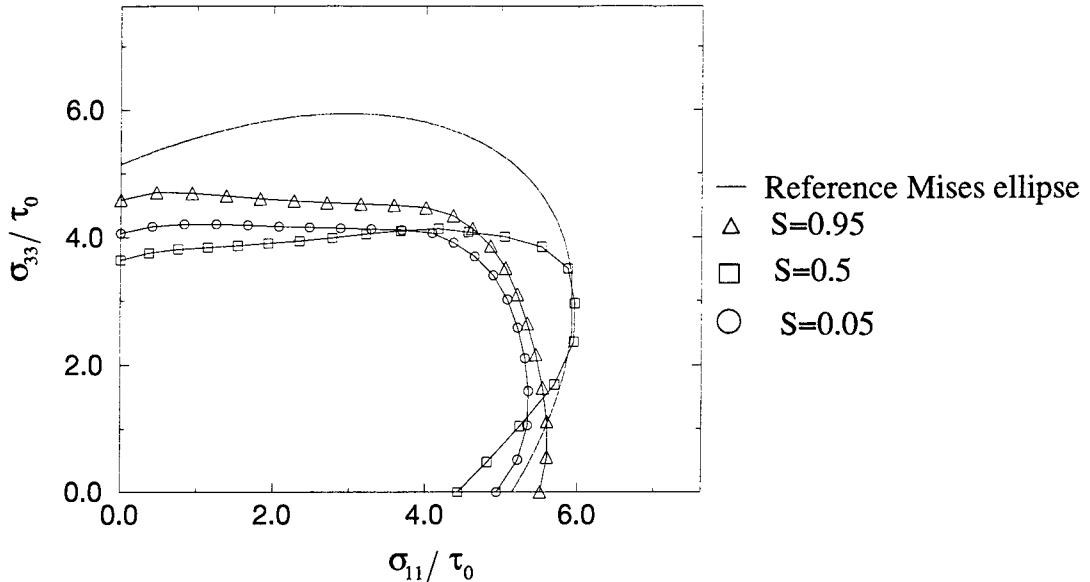
Figure 12. Constant offset effective plastic strain yield surfaces through the thickness due to 65% thickness reduction by small draught rolling with $\mu = 0.2$.

midpoint texture appears to be rotated approximately 7° too far about the transverse direction, indicating that the finite element simulation overestimated the shear penetration to the midpoint of the workpiece thickness. The experiment shows several peaks in the workpiece center that do not exist in the calculation. We note that the sheet used in this experiment was initially hot-rolled and then annealed. This previous processing left the material with strong textural peaks in the center of the sheet, which are reflected in Figure 13(b). Such peaks should not be expected to appear in a calculation which assumes initially random orientation of crystallites. It should be noted here that in modeling these experiments, the exact experimental roll-gap geometry was not simulated. Neither experiment maintained a constant roll-gap geometry, but they both were conducted within the large draught rolling regime, and it is expected that they should both produce similar through-thickness deformation fields. It should also be noted that frictional conditions at the sheet surface are not easily characterized and, thus, the amount of frictional shear imposed by the experiments is unknown.

In spite of the these inconsistencies between the calculated and experimental results, the general agreement of calculated peaks due to the predominant deformation modes are strong indicators that we can calculate textures for some complicated deformation states without extensive computational costs. The use of the finite element method in calculating the necessary boundary conditions was successful due, at least in part, to a reasonable approximation of global polycrystal aggregate behavior and in part to the careful consideration of roll-workpiece interaction. Further, by using the finite element method, details of the roll-gap displacement field could be resolved and correlated with texture development through the thickness.

The analysis of small draught rolling showed that the neutral point had moved to the exit

S=0.95

S=0.5

S=0.05

a)   b)
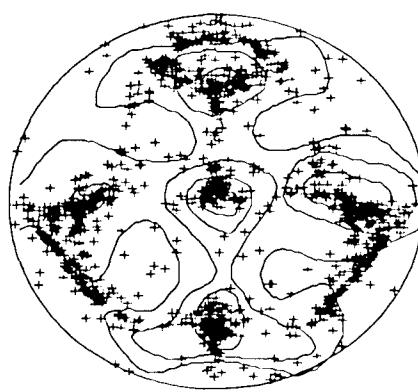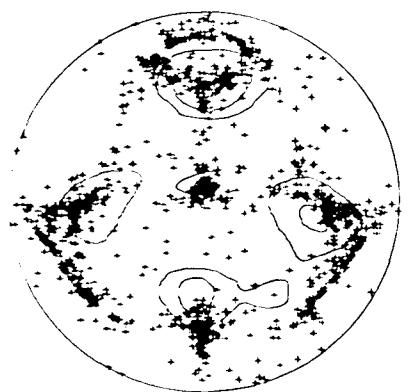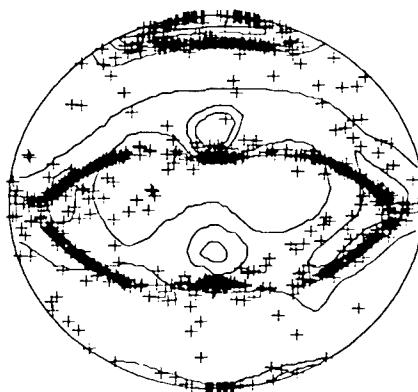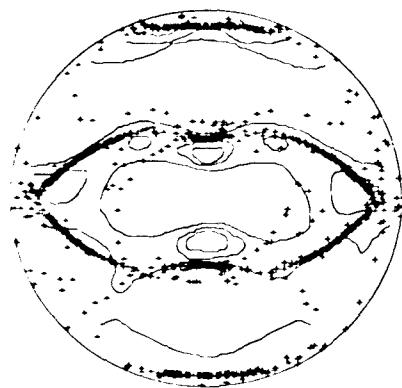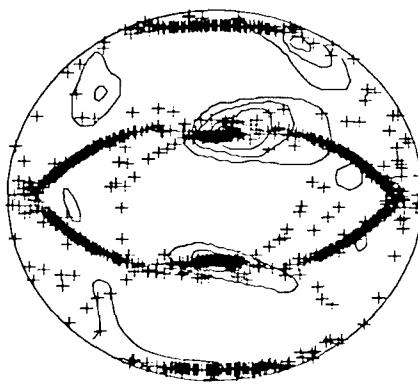
Figure 13. {111} equal-area pole figures for aluminum cold-rolled to 92%
reduction in height. The experimental results of (a) Dillamore and
Roberts (1963) and (b) Truzkowski, Krol, and Major (1980) are
shown in solid lines.

portion of the roll gap and, as a result, there was only unidirectional shearing along the interface. Due to the analysis by Hill (1950), we know that the position of the neutral point is actually a function of the coefficient of friction, and that increasing μ would result in the neutral point moving back away from the roll-gap exit. To find out whether or not the position of the neutral point would change any characteristics of the through-thickness shear inhomogeneity, the small draught model was run with μ sufficient so as to move the neutral point half way to the roll-gap entrance. Although surface shear strains were greatly increased, the reverse shearing, at S = 0.5, was maintained at roughly the same level. This led to the conclusion that the reverse shearing that is synonymous with the small draught rolling is truly a geometric effect of the roll gap and independent of the interface conditions. An examination of the flow field for the different roll gaps may prove instructive in finding the root of the textural inhomogeneity occurring in small draught rolling.

Figures 14 and 15 contain contours of maximum principal strain rate. These contour lines are a good indicator of the material flow. Figure 14 is for the entire small draught roll gap, while Figure 15(b) is for only the entrance portion of the large draught rolling case. Note that the contours for the small draught case are strikingly similar to those of the entrance portion of the large draught case. This being the case, it could be said that the small draught case is just underdeveloped (i.e., the short contact length inhibits development of the full roll-gap displacement field). Further support for this argument can be found by returning to the shear-strain time history plots for the two cases. In doing so, one would notice that the shear time history for the large draught case (Figure 6[a]), up to the normalized time of 0.2, is remarkably similar to the entire small draught shear-strain time history curve (Figure 6[c]). In other words, if one were to remove the workpiece from the roll at this time, the material would be textured as in the small draught case. Also note that the contact length scales as the square root of the roll radius, therefore, it seems that large draught displacement fields could be achieved during small reductions in thickness, provided a very large roll is used.

Our analysis shows that while frictional interaction with the roll causes a certain amount of textural inhomogeneity through the thickness, this effect is limited to the near-surface layers with only slight effects deeper in the thickness. Roll-gap geometry seems to play the major roll in determining material flow in the gap. As the length of contact between the roll and workpiece decreases, the roll-gap displacement field becomes much less uniform through the thickness. The introduction of shear strains penetrating deeper into the cross section causes rotation in the through-thickness textures to develop. These textures have profound effects on subsequent material deformation and, as a result, should be considered in the design of a final product.
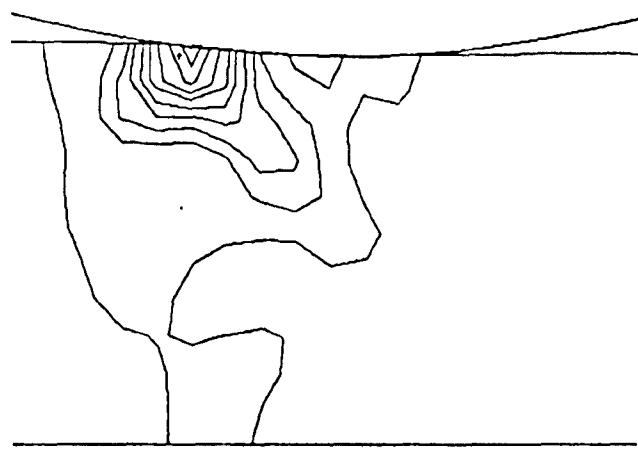
Figure 14. Contours of maximum principal strain for small draught rolling with $\mu = 0.2$.
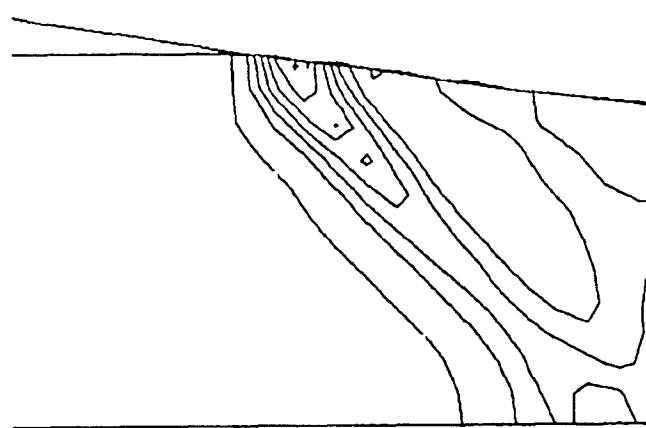

Figure 15. Contours of maximum principal strain for large draught rolling with $\mu = 0.2$.

6. References

1. Asaro, R. J., and A. Needleman, "Texture Development and Strain Hardening in Rate Dependent Polycrystals," *Acta Metallurgica et materialia*, vol. 33, no. 6, p. 923, 1985.

2. Asbeck, H. O. and H. Mecking, "Influence of Friction and Geometry of Deformation on Texture Inhomogeneities During Rolling of CU Single Crystals as an Example," *Material Science in Engineering*, vol. 34, p. 111, 1978.

3. Bammann, D. J., "Modeling Temperature and Strain Rate Dependent Large Deformations of Metal," *Applied Mechanics Review*, vol. 45, no. 5, p. 5312, 1990.

4. Benson, D. and J. Hallquist, "A Single Surface Contact Algorithm for the Post-Buckling Analysis of Shell Structures," *International Journal of Numerical Methods in Engineering*, vol. 78, p. 141, 1990.

5. Dillamore, I. L., and W. T. Roberts, "Crystallographic Texture Variations Through Rolled Aluminum and Copper Sheet," *Journal of the Institute of Metals*, vol. 92, p. 193, 1963.

6. Durham, D., and A. Assempoor, "A Comparison of Friction Models in Material Forming Processes," *Computer Modeling and Simulation of Manufactureing Processes*, AMSE Materials Division, p. 293, 1990.

7. Hallquist, J. O., "Theoretical Manual for DYNA3D," *UCID 19401*, 1982.

8. Harren, S. V., H. E. Dève, and R. J. Asaro, *Acta Metallurgica et materialia*, vol. 36, p. 2435, 1988.

9. Hibbitt, Karlsson, and Sorensen, *ABAQUS Reference Manuals*, Providence, RI, 1988.

10. Hill, R., "The Mathematical Theory of Plasticity," *Oxford Science Publications*, Oxford, 1950.

11. Hill, R. and L. Havner, "Perspectives in the mechanics of elastoplastic crystals", *Journal of Mechanics and Physics of Solids*, vol. 23, p. 239, 1975.

12. Kalidindi, S., C. Bronkhorst, and L. Anand, "Crystallographic Texture Evolution in Bulk Deformation Processing of FCC Metals," *Journal of Mechanics and Physics of Solids*, vol. 40, p. 537, 1991.

13. Kiuchi, N. and J. T. Oden, "Contact Problems in Elasticity: A study of Variational Inequalities and Finite Element Methods for a Class of Contact Problems in Elasticity," *SIAM Studies*, vol. 8, 1986.

14. Lee, C. S. and B. J. Duggan, "A Simple Theory for the Development of Inhomogeneous Rolling Textures," *Metallurgical and Materials Transactions A.*, vol. 22A, p. 2637, 1991.

15. Lequeu, P., and J. Jonas, "A Texture Based Interpretation of Optimum Drawability and Anomalous Behavior in Sheet Metals," *ICOTOM 8*, p. 1091, 1988.

16. Mathur, K., and P. Dawson, "On Modeling the Development of Crystallographic Texture in Bulk Forming Processes," *International Journal of Plasticity*, vol. 5, p. 67, 1989.

17. Nelson. K.. and W. Fricke, "Correlation of Earing in Hot Rolled 3004 Aluminum with the Crystallite Orientation Distribution Function," *ICOTOM 8*, p. 1097, 1988.

18. Peirce, D.. R. J. Asaro, and A. Needleman, "Material Rate Dependence and Localized Deformations in Crystalline Solids," *Acta Metallurgica et materialia*, vol. 31, p. 1951, 1983.

19. Richelsen. A. B., "Viscoplastic Analysis of Plane Strain Rolling Using Different Friction Models," *International Journal of Mechanical Science*, vol. 33, p. 761, 1991.

20. Schoenfeld. S. E., R. J. Asaro, D. Bammann, and D. Benson, "A Comparison of Micromechanically Based Plasticity Models," *IUTAM Symposium on Constitutive Relations for Finite Deformation of Polycrystalline Metals*, 1991.

21. Truszkowski. W., J. Krol, and B. Major, "Inhomogeneity of Rolling Texture in FCC Metals," *Metallurgical and Materials Transactions A.*, vol. 11A, p. 749, 1980.

22. Truszkowski. W. and J. Kiel. "On Penetration of Shear Texture into the Rolled Aluminum and Copper," *Metallurgical and Materials Transactions A.*, vol. 13A, p. 665, 1982.

23. Wanheim. T., "Friction at High Normal Pressures," *Annals of Wear*, vol. 25, p. 225, 1973.

24. Wanheim. T., and N. Bay. "A Model for Friction in Metal Forming Processes," *Annals of CIRP*, vol. 27, p. 189, 1978.

NO. OF COPIES	ORGANIZATION

NO. OF COPIES	ORGANIZATION

2   DEFENSE TECHNICAL
    INFORMATION CENTER
    DTIC DDA
    8725 JOHN J KINGMAN RD
    STE 0944
    FT BELVOIR VA 22060-6218

1   HQDA
    DAMO FDQ
    DENNIS SCHMIDT
    400 ARMY PENTAGON
    WASHINGTON DC 20310-0460

1   CECOM
    SP & TRRSTRL COMMCTN DIV
    AMSEL RD ST MC M
    H SOICHER
    FT MONMOUTH NJ 07703-5203

1   PRIN DPTY FOR TCHNLGY HQ
    US ARMY MATCOM
    AMCDCG T
    M FISETTE
    5001 EISENHOWER AVE
    ALEXANDRIA VA 22333-0001

1   PRIN DPTY FOR ACQUSTN HQS
    US ARMY MATCOM
    AMCDCG A
    D ADAMS
    5001 EISENHOWER AVE
    ALEXANDRIA VA 22333-0001

1   DPTY CG FOR RDE HQS
    US ARMY MATCOM
    AMCRD
    BG BEAUCHAMP
    5001 EISENHOWER AVE
    ALEXANDRIA VA 22333-0001

1   DPTY ASSIST SCY FOR R&T
    SARD TT   T KILLION
    THE PENTAGON
    WASHINGTON DC 20310-0103

1   OSD
    OUSD(A&T)/ODDDR&E(R)
    J LUPO
    THE PENTAGON
    WASHINGTON DC 20301-7100

1   INST FOR ADVNCD TCHNLGY
    THE UNIV OF TEXAS AT AUSTIN
    PO BOX 202797
    AUSTIN TX 78720-2797

1   USAASA
    MOAS AI   W PARRON
    9325 GUNSTON RD STE N319
    FT BELVOIR VA 22060-5582

1   CECOM
    PM GPS   COL S YOUNG
    FT MONMOUTH NJ 07703

1   GPS JOINT PROG OFC DIR
    COL J CLAY
    2435 VELA WAY STE 1613
    LOS ANGELES AFB CA 90245-5500

1   ELECTRONIC SYS DIV DIR
    CECOM RDEC
    J NIEMELA
    FT MONMOUTH NJ 07703

3   DARPA
    L STOTTS
    J PENNELLA
    B KASPAR
    3701 N FAIRFAX DR
    ARLINGTON VA 22203-1714

1   SPCL ASST TO WING CMNDR
    50SW/CCX
    CAPT P H BERNSTEIN
    300 O'MALLEY AVE STE 20
    FALCON AFB CO 80912-3020

1   USAF SMC/CED
    DMA/JPO
    M ISON
    2435 VELA WAY STE 1613
    LOS ANGELES AFB CA
    90245-5500

1   US MILITARY ACADEMY
    MATH SCI CTR OF EXCELLENCE
    DEPT OF MATHEMATICAL SCI
    MDN A MAJ DON ENGEN
    THAYER HALL
    WEST POINT NY 10996-1786

NO. OF
COPIES ORGANIZATION

1   DIRECTOR
    US ARMY RESEARCH LAB
    AMSRL CS AL TP
    2800 POWDER MILL RD
    ADELPHI MD 20783-1145

1   DIRECTOR
    US ARMY RESEARCH LAB
    AMSRL CS AL TA
    2800 POWDER MILL RD
    ADELPHI MD 20783-1145

3   DIRECTOR
    US ARMY RESEARCH LAB
    AMSRL CI LL
    2800 POWDER MILL RD
    ADELPHI MD 20783-1145

    ABERDEEN PROVING GROUND

4   DIR USARL
    AMSRL CI LP (305)

NO. OF COPIES	ORGANIZATION	NO. OF COPIES	ORGANIZATION

2	DIRECTOR
	LLNL
	L-170 D LASSILA
	L-355 A SCHWARTZ
	P O BOX 808
	LIVERMORE CA 94550
			AMSRL-WM-TC (continued),
			    R SUMMERS
			    W WALTERS
			AMSRL-WM-TA,
			    S BILYK
			    W BRUCHEY
			    G BULMASH

1	NSWC
	INDIAN HEAD DIVISION
	R K GARRET JR
	BLDG 841 RM 20
	101 STRAUSS AVE
	INDIAN HEAD MD 20640
			M BURKINS
			    J DEHN
			    G FILBEY
			    W GILLICH
			    W GOOCH
			    D HACKBARTH
			    T HAVEL

1	NSWC
	CARDEROCK DIVISION
	JOHN MCKIRGAN
	9500 MACARTHUR BLVD
	WEST BETHESDA MD 20817-5700
			E HORWATH
			    Y HUANG
			    H MEYER
			    E RAPACKI
			    J RUNYEON
			    N RUPERT

1	COMMANDER
	US ARMY ARDEC
	ATTN AMSTA AR FSA E
	E BAKER
	PICATINNY ARSENAL NJ
	07806-5000
			M ZOLTOSKI
			AMSRL-WM-WD, A NIILER
			AMSRL-WM-MF,
			    S CHOU
			    D DANDEKAR
			    R RAJENDRAN
			    T WEERASOORIYA
			    D GROVE

	ABERDEEN PROVING GROUND		AMSRL-WM-M, D VIECHNICKI

68	DIR, USARL
	AMSRL-WM-T, W MORRISON
	AMSRL-WM-TD,
	    A DIETRICH
	    T FARRAND
	    K FRANK
	    S SCHOENFELD (12 CP)
	    A GUPTA
	    M RAFTENBERG
	    M SCHEIDLER
	    S SEGLETES
	    J WALTER
	    T WRIGHT
	AMSRL-WM-TC,
	    W DE ROSSET
	    K KIMSEY
	    M LAMPSON
	    L MAGNESS
	    D SCHEFFLER
	    G SILSBY
			J MCCAULY
			    G HAGNAUER
			AMSRL-WM-ME,
			    M WELLS
			    R ADLER
			    M STAKER
			AMSRL-WM-MC,
			    M CHEN
			    G GILDE
			    P HUANG
			    T HYNES
			    J SWAB
			    J WELLS
			    J CASALVIA
			    C HUBBARD
			    M COLE

INTENTIONALLY LEFT BLANK

REPORT DOCUMENTATION PAGE

Form Approved
OMB No. 0704-0188

1. AGENCY USE ONLY *(Leave blank)*	2. REPORT DATE October 1997	3. REPORT TYPE AND DATES COVERED Final, September 1994 - September 1995

4. TITLE AND SUBTITLE

Through-Thickness Texture Gradients in Rolled Polycrystalline Alloys

5. FUNDING NUMBERS

61102AH43

6. AUTHOR(S)

S. E. Schoenfeld and R. J. Asaro*

7. PERFORMING ORGANIZATION NAME(S) AND ADDRESS(ES)

U.S. Army Research Laboratory
ATTN: AMSRL-WM-TD
Aberdeen Proving Ground, MD 21005-5066

8. PERFORMING ORGANIZATION REPORT NUMBER

ARL-TR-1531

9. SPONSORING/MONITORING AGENCY NAMES(S) AND ADDRESS(ES)

10.SPONSORING/MONITORING AGENCY REPORT NUMBER

11. SUPPLEMENTARY NOTES

*Current address for R. J. Asaro: Department of Applied Mechanics and Engineering Sciences, Mail Code R-011, University of California, San Diego, La Jolla, CA 92093.

12a. DISTRIBUTION/AVAILABILITY STATEMENT

Approved for public release; distribution is unlimited.

12b. DISTRIBUTION CODE

13. ABSTRACT *(Maximum 200 words)*

A simple and accurate approach to modeling deformation processes that are highly constrained by boundary conditions is presented. The method involves a detailed finite element analysis of the most controlling aspects of the process. Additional analysis of the material states of texture and anisotropy are calculated as deemed necessary. The method is applied to the rolling process with a detailed analysis of the rolling of aluminum sheet. Particular attention is paid to the analysis of the roll-gap geometry and the transfer of tractions from the roll to the workpiece. The calculated deformation state is then applied to a more detailed calculation of material texture, which tracks the motion of individual crystalites due to macroscopic boundary conditions. The method not only allows a detailed analysis of through-thickness texture gradients, but also a detailed description of the boundary conditions and deformation states that cause such textures. The macroscopic anisotropy resulting from such textures is investigated, and the use of the method as a process design tool is discussed. Finally, results are compared to experimentally determined through-thickness texture gradients in rolled aluminum alloys, and details concerning the general roll-gap deformation field are discussed.

14. SUBJECT TERMS

mechanical processing, texture evolution, anisotropy

15. NUMBER OF PAGES
39

16. PRICE CODE

17. SECURITY CLASSIFICATION OF REPORT UNCLASSIFIED	18. SECURITY CLASSIFICATION OF THIS PAGE UNCLASSIFIED	19. SECURITY CLASSIFICATION OF ABSTRACT UNCLASSIFIED	20. LIMITATION OF ABSTRACT UL

NSN 7540-01-280-5500

Standard Form 298 (Rev. 2-89)
Prescribed by ANSI Std. 239-18   298-102

INTENTIONALLY LEFT BLANK

USER EVALUATION SHEET/CHANGE OF ADDRESS

This Laboratory undertakes a continuing effort to improve the quality of the reports it publishes. Your comments/answers to the items/questions below will aid us in our efforts.

1. ARL Report Number/Author ARL-TR-1531 (Schoenfeld) Date of Report October 1997

2. Date Report Received _____

3. Does this report satisfy a need? (Comment on purpose, related project, or other area of interest for which the report will be used.) _____

_____

_____

4. Specifically, how is the report being used? (Information source, design data, procedure, source of ideas, etc.) _____

_____

_____

5. Has the information in this report led to any quantitative savings as far as man-hours or dollars saved, operating costs avoided, or efficiencies achieved, etc? If so, please elaborate. _____

_____

_____

6. General Comments. What do you think should be changed to improve future reports? (Indicate changes to organization, technical content, format, etc.) _____

_____

_____

_____

	Organization	
CURRENT ADDRESS	Name	E-mail Name
	Street or P.O. Box No.	
	City, State, Zip Code	

7. If indicating a Change of Address or Address Correction, please provide the Current or Correct address above and the Old or Incorrect address below.

	Organization
OLD ADDRESS	Name
	Street or P.O. Box No.
	City, State, Zip Code

(Remove this sheet, fold as indicated, tape closed, and mail.)
(DO NOT STAPLE)